RSC Advances

PAPER

View Article Online
View Journal | View Issue

Cite this: *RSC Adv.*, 2025, **15**, 32131

Delithiation effects on the structural, electronic, and electrical properties of $LiSr_{0.8}Fe_{0.1}Ni_{0.1}PO_4$ material

A. Mabrouki, *[a] Olfa Messaoudi,[b] Lamia Trabelsi,[c] Moufida Mansouri[d] and Latifah Alfhaid[b]

Received 26th April 2025
Accepted 27th August 2025

DOI: 10.1039/d5ra02943k

rsc.li/rsc-advances

In the scope of designing Li-ion batteries with increased energy density, developing new high-performance, stable, and inexpensive cathode materials remains a significant challenge. In this context, the $LiSr_{0.8}Ni_{0.1}Fe_{0.1}PO_4$ material was synthesized and systematically investigated. Using Density Functional Theory (DFT) calculations, the structural stability and electronic structure were investigated during the delithiation process. The results indicate the stability of the compound during the deintercalation process and revealed a change from semiconducting to semi-metallic behavior. The expected voltage window for this material is between 3.4 and 3.25 V. A comprehensive electrical study was conducted to analyze the conduction mechanism, which is governed by the correlated barrier hopping (CBH) model below 370 K, and the non-overlapping small polaron tunneling (NSPT) model above 370 K. The consistent values of the estimated activation energy related to both conduction and impedance variation prove that the relaxation and conduction processes are governed by the same mechanism.

1. Introduction

Rechargeable batteries play a critical role in the advancement of energy storage technologies, particularly in addressing the increasing demand for power and the need for sustainable energy solutions. These batteries have become essential components in various applications, ranging from portable electronics to electric vehicles and grid-level energy storage systems.[1,2]

Among the various battery technologies, lithium-sulfur batteries with a high theoretical energy density of 2600 Wh kg^{-1},[3] lithium-ion batteries (LIBs),[4–6] and hydrogen storage materials have attracted significant attention. Over the past 20 years, extensive research has been conducted on interstitial hydrides, elemental hydrides, and complex hydrides.[7–10]

Nowadays, LIBs play a crucial role and have become the leading technology in the rechargeable battery market, particularly due to the increasing demand for electric vehicles. This demand has driven substantial efforts to improve energy and power density, leading to the emergence of various chemistries for both cathodes and anodes.

Among LIBs, $LiFePO_4$ (LFP) batteries are highly promising owing to their longer lifespan, safety, environmental friendliness, and reliability.[11] They were discovered by A. K. Padhi *et al.* and have a theoretical capacity of 170 mA h g^{-1}.[12] Their demand is experiencing rapid growth especially as they are used for EVs and are also being used in grid-scale energy storage systems due to their ability to handle frequent charge and discharge cycles. According to the TrendForce 2022 Lithium Battery Market Analysis Report, the market share of $LiFePO_4$ increased from 27% in 2019 to 46% in 2022 and expected to reach 64% in 2025.[13]

The absence of expensive and critical elements such as Co, Ni, and Mn in LFP batteries makes them interesting despite their lower power density, capacity, and specific energy. Additionally, LFP batteries are less vulnerable to thermal runaway than NMC batteries when damaged or defective.[14]

While LFP batteries have several advantages, their low electronic conductivity $\sim 10^{-10}$ to 10^{-7} S cm^{-1} and low Li-ion diffusivity $\sim 10^{-12}$ to 10^{-16} cm^2 s^{-1} pose challenges for their use in practical large-scale commercial applications.[15] To address these issues, substitution of the cathode elements has been proposed as one of the emerging solutions. Substitution of Fe by other metals such as Mn, Ni and Co and coating with carbon have been applied.[16–18] Research interest in Co-doping $LiFePO_4$ composites has been strongly developed and has been considered one of the most significant methods of modification to improve LFP performances.

Li *et al.* prepared V–F co-doped LFP/C and studied in detail the intrinsic structure.[19] They found that vanadium ion doping

[a]*Laboratory of Applied Physics, Faculty of Sciences of Sfax, University of Sfax, B.P. 1171, 3000 Sfax, Tunisia. E-mail: mabroukiala1993@gmail.com*

[b]*Physics Department, College of Sciences, University of Ha'il, P. O. Box 2440, Ha'il, Saudi Arabia*

[c]*Computer Science Department, Applied College, University of Ha'il, Ha'il 55424, Saudi Arabia*

[d]*Sfax University, B.P. 1171, 3000 Sfax, Tunisia*

improved both ionic and electronic conductivities without directly affecting the electrochemical reaction. Consequently, the kinetic restriction in the olivine LFP structure may be alleviated in some way by the doping.[20] Shu *et al.* have investigated LFP doped with Na and Ti. Na and Ti co-doping was observed to enhance the electrochemical properties of $LiFePO_4$/C cathode materials.[21] The $Li_{0.97}Na_{0.03}Fe_{0.97}Ti_{0.03}PO_4$/C composition exhibited an initial discharge capacity of 151.0 mA h g^{-1}, with a capacity retention ratio of 99.3% after 100 cycles at 1 °C. Notably, even at a high discharge rate of 20 °C, it maintained a discharge capacity of over 97.3 mA h g^{-1}.[21]

Density Functional Theory (DFT) first-principles computations have proven to be highly effective in predicting various properties of Li-insertion materials used as electrodes in rechargeable lithium-ion batteries. In this work, $LiSr_{0.8}Fe_{0.1}Ni_{0.1}PO_4$ compound was prepared using a simple sol gel method. To explore the impact of Li deintercalation on its structural and the electronic properties, DFT calculations were performed. The electrical and electrochemical properties of $LiSr_{0.8}Fe_{0.1}Ni_{0.1}PO_4$ composites were studied in detail.

2. Experimental and computational details

2.1. Experimental details

The sol–gel process was used to synthesize $LiSr_{0.8}Fe_{0.1}Ni_{0.1}PO_4$ oxide. Stoichiometric amounts of $LiNO_3$, Sr $(NO_3)_2$, $(NH_4)H_2PO_4$, Fe $(NO_3)_3 \cdot 9H_2O$, Ni $(NO_3)_2 \cdot 6H_2O$ were used. Initially, the precursors were dissolved individually in 50 mL of distilled water at 70 °C. By adding a mixture of citric acid ($C_6H_8O_7$) and ethylene glycol ($C_2H_6O_2$) with a 1/1.5 mol ratio, a homogenous solution was formed. This solution was then slowly evaporated until it formed a gel. The gel was heated at 150 °C and the temperature was gradually increased until a foam-like powder was obtained. Then, the powder was ground, pelletized, and finally annealed at 650 °C for 7 h.

The crystal structure of $LiSr_{0.8}Fe_{0.1}Ni_{0.1}PO_4$ sample was determined using a Bruker D8 diffractometer operating with CuKα radiation ($\lambda = 1.542$ Å). The morphological properties of the compound were studied using a TESCAN VEGA3 scanning electron microscope (SEM). The dielectric measurements were performed using a Tegam 3550 ALF impedance analyzer.

2.2. Computational details

All DFT calculations were performed using the WIEN2k Simulation Package.[22] To numerically study $LiSr_{0.8}Fe_{0.1}Ni_{0.1}PO_4$ sample, we created a supercell containing 32 Li atoms, 16 Sr atoms, 3 Fe atoms, 3 Ni atoms, 32 P atoms and 128 O atoms). The $Li_{1-x}Sr_{0.8}Fe_{0.1}Ni_{0.1}PO_4$ structure were modeled by removing the correspond Li atoms. The electrons in the 3d and 4f elements are known to be influenced by a strong Coulomb interaction. To account for the strongly correlated nature of the d electrons of Ni and Fe ions, the Hubbard (U) correction was applied, resulting to the GGA + U approach.[23,24] The accuracy of GGA + U calculations is influenced by the choice of the Hubbard U parameter, which varies depending on the valence state of the transition metal and its surrounding crystal environment. This U value can be determined from first principles using linear response theory,[25,26] or alternatively, it can be empirically tuned to reproduce key material properties, such as the electronic band gap or lithium insertion potential.[27–29,37,38]

In our work, we adopted $U = 5.3$ eV for Fe ions[28,30,30,31] and $U = 6.0$ eV for Ni ions,[32,33] which are values commonly used in previous studies of olivine-type phosphates and similar transition metal oxide compounds. These values were not arbitrarily chosen but rather selected based on a combination of literature precedent and their established ability to reproduce experimentally observed structural, electronic, and electrochemical properties in similar systems.

All calculations were spin-polarized and the ferromagnetic spin ordering was initialized on the Fe and Ni ions.

The Nudged Elastic Band (NEB) was employed to calculate the activation energy (E_a) associated with Li-ion hopping.[34,35] In this approach, a series of intermediate images is generated between fixed initial and final positions of the diffusing ion. The initial and final configurations were used in conjunction with the climbing image method, with intermediate images spaced at intervals of 0.5 Å along the diffusion path. Our approach considers only the diffusion of the Li ion. This method efficiently identifies the energy saddle point associated with ion diffusion.

In order to estimate the activation energy barrier (E_a)) calculations were performed. The initial and final configurations were used in conjunction with the climbing image method, with intermediate images spaced at intervals of 0.5 Å along the diffusion path. Our approach considers only the diffusion of the Li ion.

To obtain precise total DFT energies, a 500 k-point mesh were used. In all cases, the structures were optimized and fully relaxed. The convergence criteria were set as follows: the energy threshold was 10^{-4} Ry and the force threshold was Ry $Å^{-1}$.

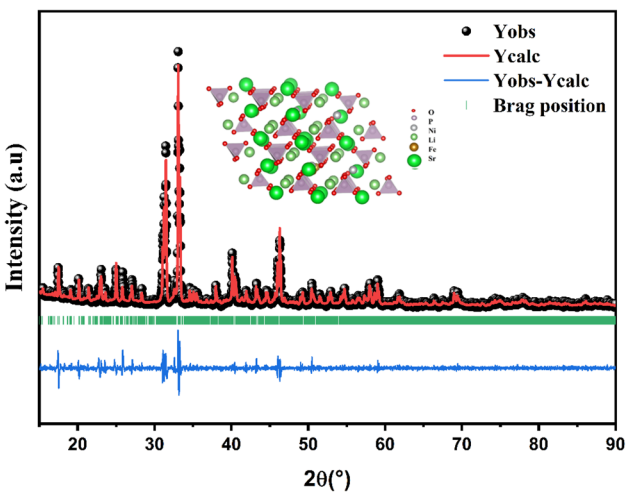

Fig. 1 Rietveld refinement of X-ray diffraction data for the $LiSr_{0.8}Fe_{0.1}Ni_{0.1}PO_4$ powder sample. The inset of figure presents the crystal structure of $LiSr_{0.8}Fe_{0.1}Ni_{0.1}PO_4$.

Table 1 Experimental and calculated lattice parameters of $Li_{1-x}Fe_{0.1}Ni_{0.1}SrPO_4$ ($x = 0$, 0.25, 0.5, 0.75, 1) where x is the amount of deintercalated Li

	a (Å)	b (Å)	c (Å)	a deviation (%)	b deviation (%)	c deviation (%)	β (°)	V (Å^3)
$x = 0$ (exp)	16.201_9	11.844_1	13.201_8				118.4413	2227.5996
$x = 0$	15.811_9	11.983_8	12.891_7				118.12375	2154.3868
$x = 0.25$	15.6221_6	11.839_9	12.856_8	1.2	1.2	0.27	117.8641	2102.3713
$x = 0.5$	15.622_1	11.839_9	12.856_8	1.65	1.4	0.1	117.81338	2103.3543
$x = 0.75$	15.416_6	11.875_9	12.788_5	2.5	0.9	0.8	117.24134	2081.7227
$x = 1$	15.464_1	11.768_1	12.646_7	2.2	1.8	1.9	116.7308	2055.5250

3. Results and discussions

3.1. Structural and morphological study

The XRD analysis using Rietveld method with the Fullproof program (Fig. 1) confirms that the sample crystallizes in the monoclinic structure with the $P2/m$ space group. The inset of Fig. 1 shows a representative crystal structure of the $LiSr_{0.8}Fe_{0.1}Ni_{0.1}PO_4$ sample, which appears to be slightly distorted. No additional impurity peaks were detected, confirming the absence of secondary phases in the compound.

Table 1 presents the computed structural characteristics of $LiSr_{0.8}Fe_{0.1}Ni_{0.1}PO_4$. The optimized lattice parameters a, b, and c, are within 3% of the experimental data. The minor discrepancies between the experimental and theoretical values validate the adopted method. To study the structural stability and understand structural evolution during delithiation, the process of Li extraction from the $LiSr_{0.8}Fe_{0.1}Ni_{0.1}PO_4$ lattice is examined using DFT calculations. Each extraction phase involves the removal of a specific amount of Li, followed by the relaxation of the resultant structure. The small variations of the lattice parameters during the extraction of Li from $Li_{1-x}Sr_{0.8}Fe_{0.1}Ni_{0.1}PO_4$ ($x = 0$, 0.25, 0.5, 0.75, 1) demonstrate that structural stability is successfully maintained throughout the different phases. After complete Li extraction ($x = 1$), the structure exhibits a 7% change in cell volume, suggesting enhanced stability compared to other compounds.[36,37]

Fig. 2(a) shows SEM images of Li $Sr_{0.8}Fe_{0.1}Ni_{0.1}PO_4$ sample. The particles are seen to have a spherical form with a wide range of particle sizes. A Gaussian fit is used to alter the size distribution histogram (Fig. 2b). The average particles size was found to be $D_{SEM} = 198$ nm.

4. Electronic properties

4.1. Optical properties

The densities of states (DOS) were analyzed to estimate the electronic conductivity of the $Li_{1-x}Sr_{0.8}Fe_{0.1}Ni_{0.1}PO_4$ systems in the spin-polarized state. Total and partial orbital DOS are shown in Fig. 3. In all cases, the density of states is dominated by Fe/Ni (3d) and O 2p states, with only minor contributions from Li (2s), P (3p) and Sr (3d) near Fermi states. The initial $LiSr_{0.8}Fe_{0.1}Ni_{0.1}PO_4$ structure was found to be a magnetic insulator exhibiting a band gap of $E_g1 = 1.4$ eV for spin-down states and $E_g2 = 2.5$ eV for spin-up states.

The experimental band gap energy value (E_g) was estimated using Tauc relation[38,39] by plotting the variation of $[\alpha h\nu]^{1/2}$ as a function of the photon energy $[h\nu]$ as shown in Fig. 4.

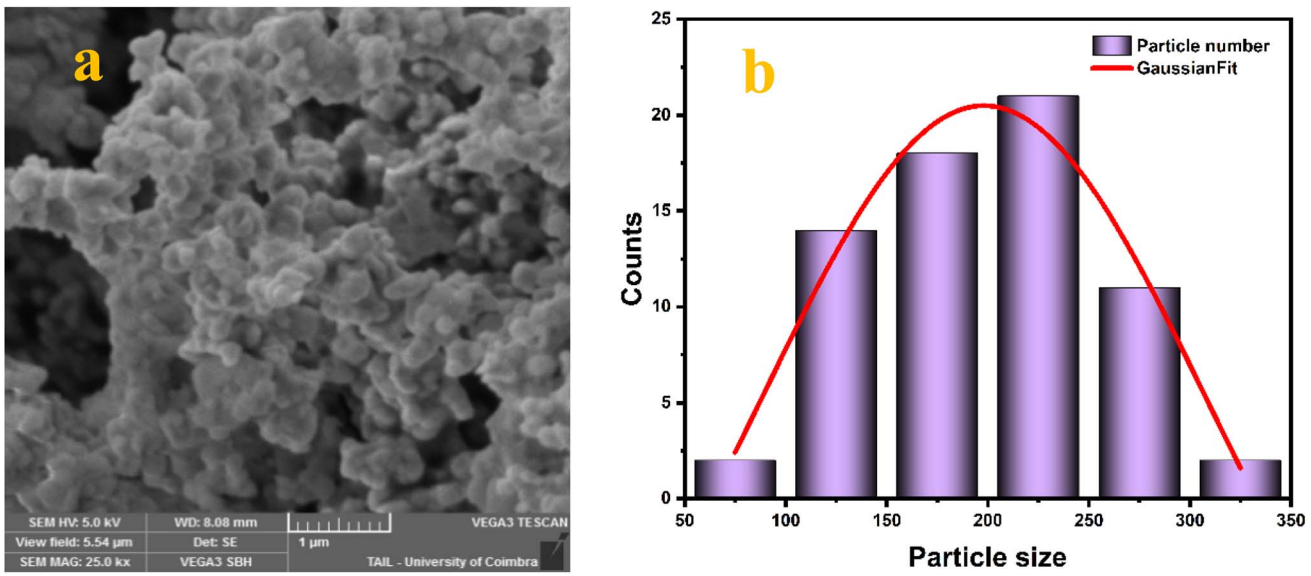

Fig. 2 (a) SEM image for Li $Sr_{0.8}Fe_{0.1}Ni_{0.1}PO_4$ sample, (b) particles size distribution.

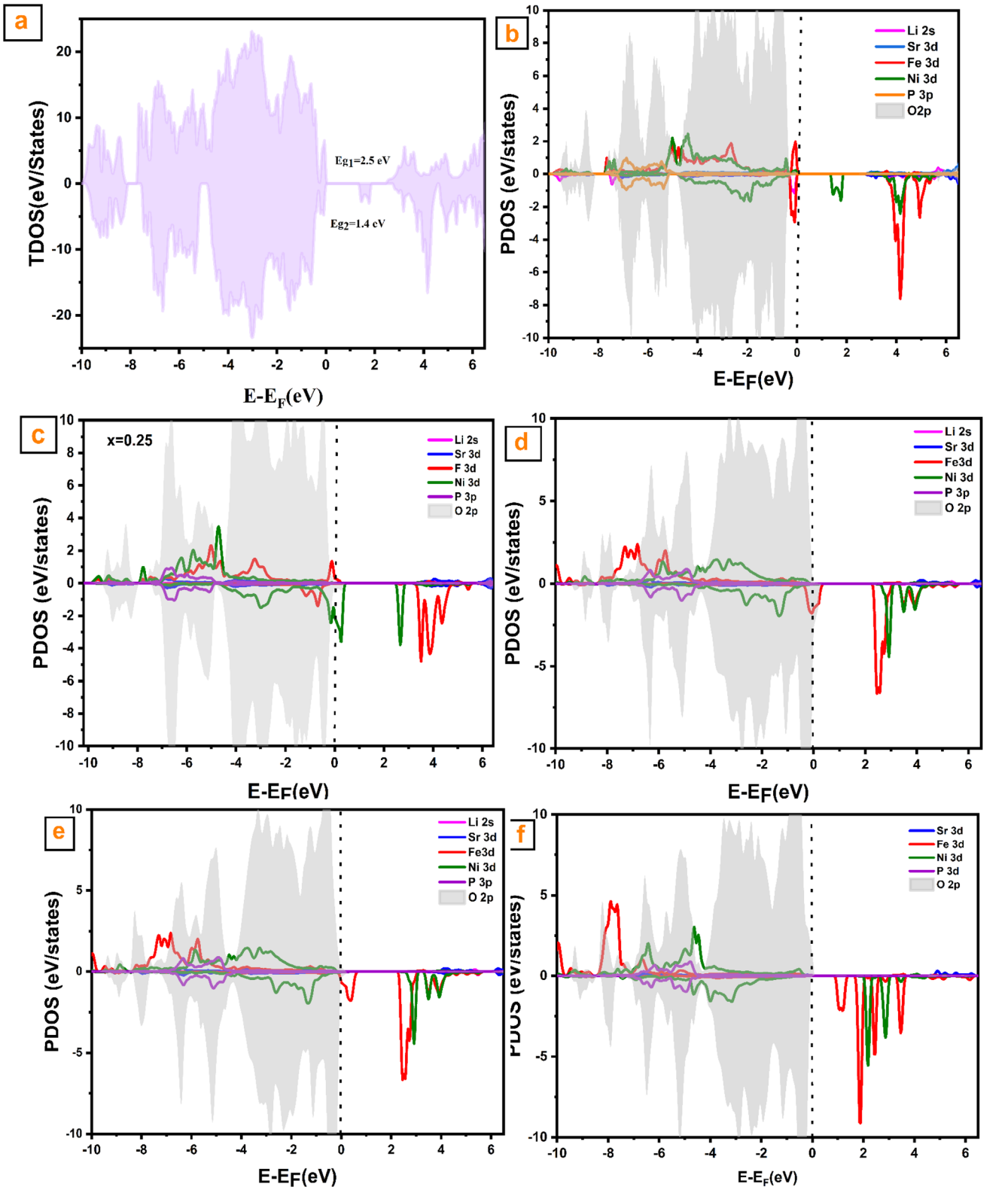

Fig. 3 Spin polarized calculated DOS) of $Li_{1-x}Sr_{0.8}Fe_{0.1}Ni_{0.1}PO_4$: total DOS (a) partial DOS of $Li_{1-x}Sr_{0.8}Fe_{0.1}Ni_{0.1}PO_4$, ((b)$x = 0$, (c) $x = 0.25$, (d) $x = 0.5$, (e) $x = 0.75$, and (f) $x = 1$.

$$(\alpha h\nu) = A[h\nu - E_g]^n \quad (1)$$

where (α) is the absorption coefficient, (E_g) is the gap energy, $(h\nu)$ is the energy of the incident radiation expressed in (eV), (A) is a constant, and (n) the exponent characterizes the type of

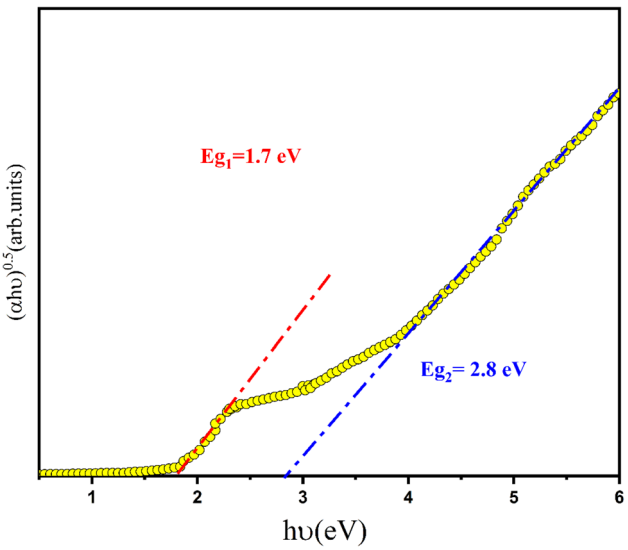

Fig. 4 Evolution of $[\alpha h\nu]^2$ *versus* $(h\nu)$ of Li $Sr_{0.8}Fe_{0.1}Ni_{0.1}PO_4$.

optical transition. However, a good agreement between experimental and theoretical results was found. In which, the experimental gap energy's (E_g) value is around 1.8 and 2.2 eV for S1 and S2 samples respectively. Our ferrite sample demonstrates semiconducting activity, according to the band gap energy value, and can be used in a variety of technical domains, including optoelectronics, photovoltaics, and photocatalysis applications.

The material becomes semi-metallic at $x = 0.25$, yielding enhanced electrical conductivity suitable for Li-ion batteries. As Li-ion extraction increases, Ni (3d) and Fe (3d) states emerge at the Fermi level for spin-down states induces a semi-metallic behavior that further enhancing electrical conductivity. The metallic character intensifies with increasing Li removal. In contrast, the fully deintercalated $Fe_{0.1}Ni_{0.1}Sr_{0.8}PO_4$ system became a magnetic semiconductor with a narrow band gap of E_g = 0.854 eV. Fig. 3 highlights the significant role of oxygen states near the Fermi level in $LiSr_{0.8}Fe_{0.1}Ni_{0.1}PO_4$. Consequently, oxygen oxidation provides the primary charge compensation mechanism during Li removal. The substantial PDOS contribution from oxygen states below E_F indicates their dominant role in the oxidation reaction – exceeding contributions from Ni and Fe. Strong hybridization between Fe (3d), Ni (3d), and O states is observed within the −4 eV to 0 eV energy range.

DOS analysis reveals that Fe–O hybridization in the empty states of the fully delithiated compound is weaker than Ni–O hybridization. Interestingly, in the pristine material ($x = 0$), states immediately below the Fermi level exhibit a dominant Fe 3d character. This suggests Fe oxidizes preferentially during initial Li extraction,[40] evidenced by a gradual shift of the Fe (3d) peak below the Fermi level toward the conduction band as Li removal increases. Conversely, in the case of $x = 0$, Ni plays a substantial role in the redox reaction, formally participating in it. When an amount of Li is removed, a noticeable redox change is observed, which is represented by the small peak above the Fermi energy linked to Fe (3d).

To gain deeper insight into the bonding nature of $LiSr_{0.8}Ni_{0.1}Fe_{0.1}PO_4$, the electronegativity differences (ΔEN) between constituent elements were evaluated using the Pauling scale. The Li–O (ΔEN = 2.46) and Sr–O (ΔEN = 2.49) bonds are primarily ionic, contributing significantly to lattice cohesion and overall structural stability.[41] The P–O bonds (ΔEN = 1.25) are polar covalent, consistent with the strong directional bonding within the PO_4^{3-} tetrahedral units, a characteristic commonly observed in phosphate-based materials.[42] In contrast, the Ni–O and Fe–O bonds (ΔEN ≈ 1.5–1.6) exhibit a mixed ionic–covalent character. This intermediate bonding regime is favorable for redox-active centers, as it facilitates efficient charge transfer while maintaining the structural integrity of the framework during Li-ion intercalation/deintercalation processes.[43,44] These results align with earlier studies on olivine and NASICON-type phosphates, where similar ΔEN trends have been linked to enhanced electrochemical performance and long-term stability.[45] Furthermore, our bonding analysis approach is in line with the methodology adopted by Sharma *et al.*,[9] who emphasized the importance of electronegativity differences in interpreting the bonding and functional properties of polyanion-based materials.

5. Electrical and dielectric properties

5.1 Electrical properties

To investigate the electrical properties of Li $Sr_{0.8}Fe_{0.1}Ni_{0.1}PO_4$ sample, the frequency dependence of conductivity was examined at various temperatures. Fig. 5 shows the evolution of AC-conductivity *versus* frequency at various temperatures [300–440 K]. The presence of two different regions indicates two different conduction phenomena. The first region corresponds to the dc-conductivity and is characterized by an independent plateau region at the low frequencies. The second one is related to the mobility of free charge carriers and represents the frequency dispersion region at higher frequencies. In this region, the conduction is affected by grains with low resistance, whereas at low frequencies the dominant role of grain boundaries having higher resistance than the grains, explains the low of ac-conductivity values.[46,47]

Fig. 5a clearly shows that as the temperature increases the frequency shifts towards a higher frequency region at which the dispersion becomes predominant. This shift can be explained by the increase mobility of charge carriers. However, it does not indicate an increase in charge concentration.[48]

The ac-conductivity can be analyzed using Jonscher's power law:[49]

$$\sigma_{ac}(\omega) = \sigma_{dc} + A(T)\omega^{s(T)} \quad (2)$$

where the first term σ_{dc}, denotes the continuous electrical conductivity related to the translational jump in long-distance electrical transport. It is temperature-dependent and remains unaffected by frequency. A is a temperature dependent parameter and represents the degree of complex interactions between mobile species,[50] 's' is an exponent depending on the temperature whose value comprises between 0 and 1.

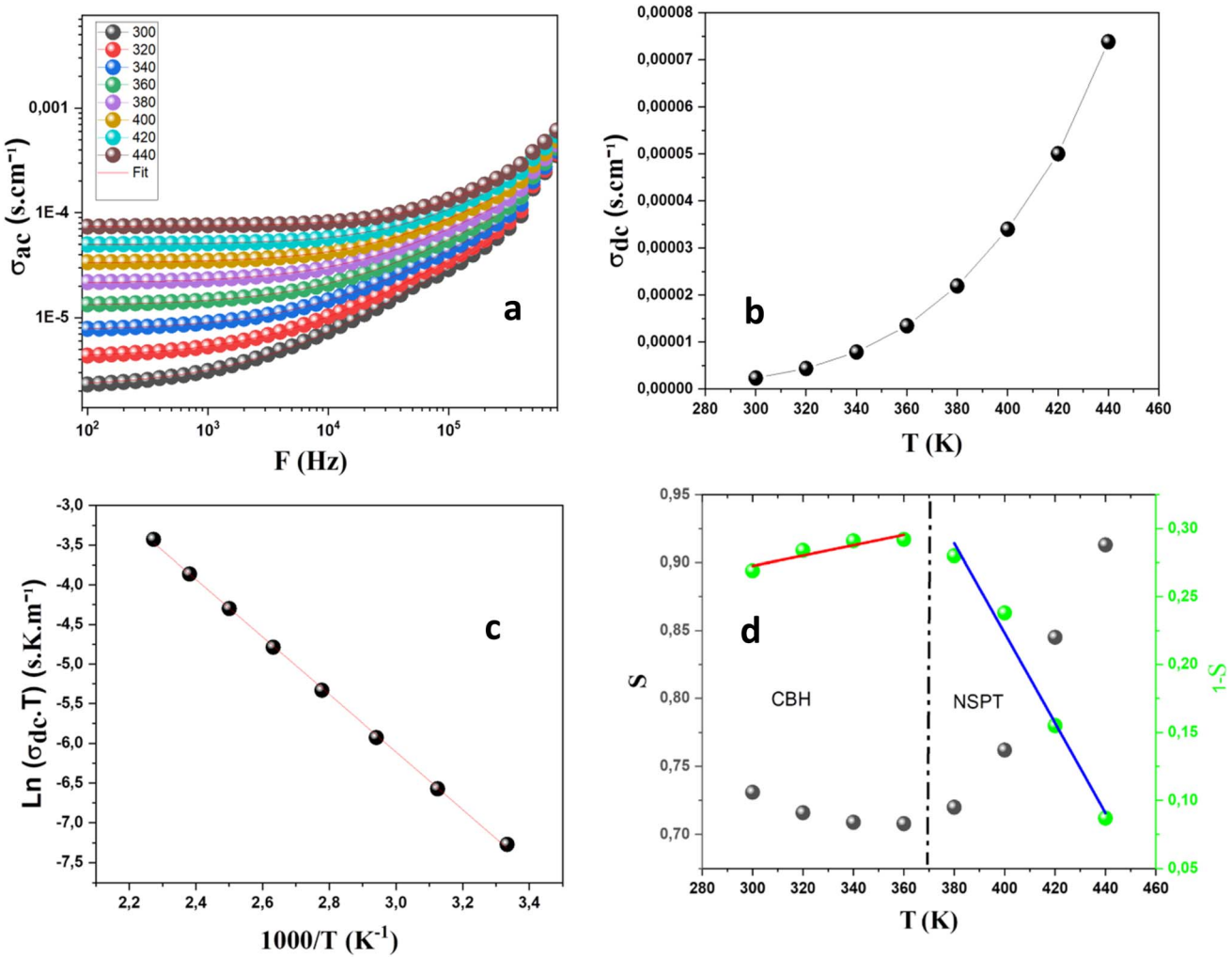

Fig. 5 (a) Evolution of conductivity *versus* frequency, (b) variation of σ_{dc} *versus*. Temperature, (c) Ln(σ_{dc}) as function of 1000/T and (d) variation of s exponent as function of temperature.

Eqn (2) was used to fit the conductivity spectra, providing an overview of the fitting results. The σ_{dc} values obtained from the best fit results are plotted as a function of temperature (Fig. 5b). The σ_{dc} conductivity was found to be enhanced as temperature rises. As the temperature rises, free carrier charges gain more energy to overcome the potential barrier, indicating a semiconducting behavior.[24] To examine the mechanism of conductivity, the evolution of Ln(σ_{dc}) according to 1000/T was plotted in Fig. 5c. The plots have been correctly fitted using Mott and David's small polaron hopping law:[51]

$$\sigma_{dc}T = \sigma_0 e^{\frac{-E_a}{K_B T}} \quad (3)$$

where E_a denotes the activation energy and σ_0 denotes pre-exponential factor. The activation energy value E_a was found to be 0.3 eV. The linear variation of Ln(σ_{dc}) with 1000/T confirms that a single conduction process occurs in this temperature range.

Fig. 5d shows the variation of exponent 's' which is used to determine the predominant conduction mechanism. Generally, the temperature dependence of 's' can be described using various theoretical models.[52,53] In Fig. 5d, it is observed that the 's' exponent decreases when T increases below 370 K, demonstrating that the conduction mechanism is guided by the correlated barrier hopping (CBH) model. Above 370 K, the exponent increases as a function of temperature, indicating that the conduction process in this temperature range is driven by non-overlapping small polaron tunneling (NSPT).[25,26] Furthermore, these values are smaller than 1. According to Funke,[54] this suggests that the electrical conduction process occurs during abrupt hopping.[55]

5.2. Impedance spectroscopy studies

The electrical properties, such as dielectric relaxation and the impedence spectroscopy were studied. The real (Z') and imaginary (Z'') parts of the complex impedance were determined using the equation:

$$Z^* = Z' - jZ'' \quad (4)$$

Fig. 6a depicts the variation of the real part (Z') of impedance as a function of frequency at different temperatures. The initial

values of Z' decrease with increasing frequency, which may be attributed to a gradual dynamic relaxation process in the material, most likely caused by the liberation of space charges. The appearance of a plateau region at high temperatures and low frequencies may be attributed to a frequency invariant electrical feature (dc-conductivity) of the material.[56]

Fig. 6b shows the imaginary component of the impedance (Z'') as a function of frequency at various temperatures. The impedance spectra are characterized by the emergence of a peak that shifts to higher frequencies with increasing temperature. The relaxation frequency, which is the frequency at which the maximum of the imaginary component of the impedance is observed, is influenced by both temperature and composition. When the temperature increases, the amplitude of the Z'' value decreases and the peak position/frequency shifts toward the higher frequency side. This means that the electrical relaxation is a thermally triggered process.[57,58] As temperature increases, the peaks broaden and the Z'' values converge at higher frequencies across all temperatures. The release/disappearance of space charge at higher frequencies is associated to the merging of the imaginary component of the impedance spectra at higher frequencies.[59] The relaxation in the present system consists of a long-term order.

The variation of $\ln(f_{max})$ as a function of $1000/T$ is shown in Fig. 6c. The activation energies of the sample were obtained by computing the slopes of the linear fit according to Arrhenius law.[60] This value is comparable to the one predicted by electrical conductivity spectra. This agreement allows us to confirm that the processes of relaxation and conduction are ensured by an identical mechanism.

The scaling behavior of Z'' is displayed in Fig. 6d at various temperatures. The two axes are normalized by their maximum values, f_{max} and Z_{max}, respectively, where f_{max} is the frequency that corresponds to Z_{max}. The dynamic processes appear to be temperature-independent as indicated by on the merging of all curves at higher frequencies at all temperatures.[57]

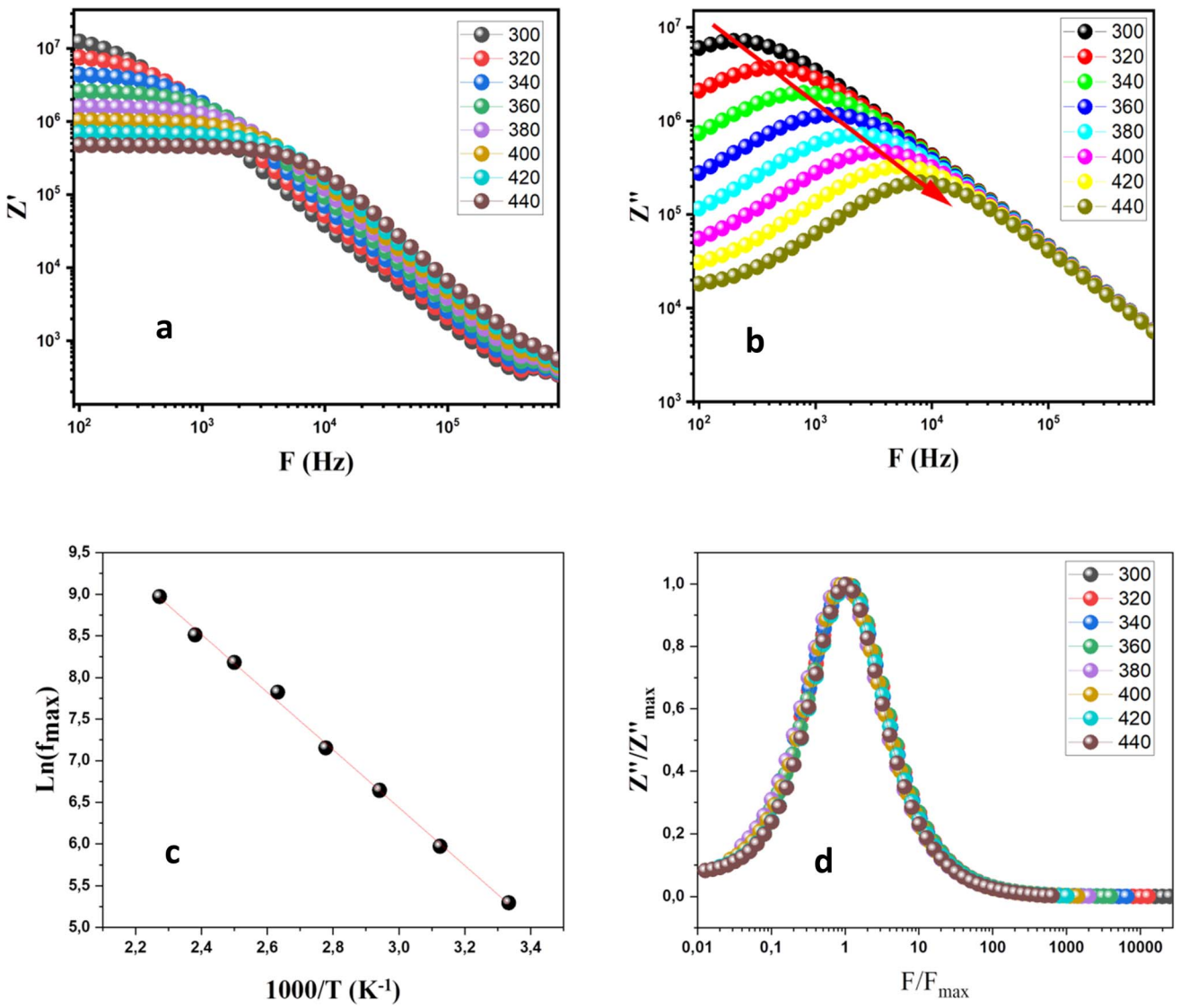

Fig. 6 Variation of the real (a) and imaginary (b) parts of the impedance as function of frequency, (c) the variation of $\ln(f_{max})$ as a function of $1000/T$, and (d) The scaling behavior of Z''/Z'.

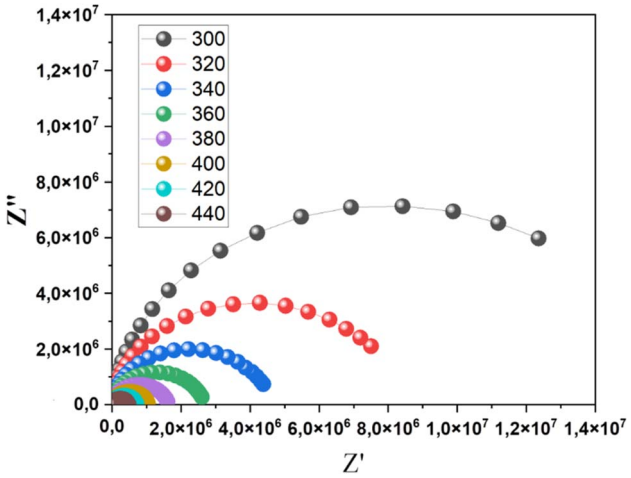

Fig. 7 Nyquist plot.

The Nyquist plot, Z'' as a function of Z', at various temperatures is shown in Fig. 7. Each temperature range reveals a complete semicircular curve. This demonstrates that the system is capable of relaxing. This might be explained by phenomena connected to grains.

Additionally, the diameter of the semicircle arcs decreases as temperature rises, reflecting a temperature-dependent decrease in electrical resistance and supporting the thermal activation of the conduction process. Furthermore, the centers of these semicircles are situated below the Z' axis and are mostly depressed, indicating that the conduction of this sample adheres to the Cole–Cole model rather than the Debye model.[61]

5.3. Electric modulus

The form of the complex electric modulus M was studied to determine the electrical properties. The complex electric modulus M is the inverse of the complex permittivity, and it is expressed as:

$$M^* = M' + jM'' \quad (5)$$

The real (M') and imaginary (M'') parts of the complex electric modulus were determined using the expressions $M' = \omega C_0 Z''$ and $M'' = \omega C_0 Z'$, where $C_0 = \varepsilon_0 A/e$, A is the area of the sample, e is the thickness of the sample and $\varepsilon_0 = 8.854 \times 10^{-14}$ F cm^{-1} is the permittivity of the free space.

Fig. 8a displays the variation of the real component of the complex modulus (M') as a function of frequency at various temperatures. The values of M' tend to approach zero at lower frequencies. This may be because long-range charge carriers in the conduction mechanism travel at these frequency ranges and electrode polarization is neglegible.[62] Additionally, a notable dispersion is observed as the frequency increases (likely approaching M'^{max}), which may be attributed to conduction phenomena related to the mobility of charge carriers at short distances.[61,63]

The imaginary part of the modulus (M'') exhibits a single relaxation peak (Fig. 8b). The peak shifts to higher frequencies as the temperature rises. This behavior implies that dielectric relaxation is thermally active, with the charge carrier hopping process dominating. The asymmetric nature of the M'' peaks implies that the material has a non-Debye response.[61] The increase in the intensity of the imaginary component of the electric modulus, M'', with rising temperature is often associated with the dielectric relaxation processes, ionic movements, and changes in the mobility of electric charges in materials.

The estimated activation energy value was obtained by linearly fitting fit (according to Arrhenius law[60]) the Ln(F_{max}) *vs.* 1000/T curve (Fig. 8c) is 0.334 eV. This value is consistent with that obtained from conductivity measurements and the jump frequency, confirming that the relaxation and conduction processes are governed by the same mechanism. The evolution of M'' *Vs.* M' is shown in Fig. 8d where a single asymmetric semicircular arc develops showing the presence of electrical relaxation processes in the material and verifying the compound's single-phase properties obtained from XRD results.[61]

6. Diffusion energy and voltages/ redox potential

The diffusion energy profiles of Li and the corresponding migration pathways between two neighboring Li sites in the $LiSr_{0.8}Ni_{0.1}Fe_{0.1}PO_4$ compound were analyzed and are presented on Fig. 9a. The calculated activation energy for Li migration is approximately 0.29 eV, which is in good agreement with the experimentally observed value in the present work.

For comparison, the experimental activation energy reported in the literature for $LiFePO_4$ ranges between 0.55 and 0.65 eV,[64] while theoretical calculations yield values between 0.3 and 0.4 eV.[35]

The presence of Sr^{2+} ions at the M site likely contributes to the widening of the Li diffusion channels due to their larger ionic radius, thereby facilitating Li^+ migration and lowering the energy barrier.

This enhanced Li mobility is a key factor for improving the electrochemical performance of cathode materials in Li-ion batteries. A lower activation energy directly correlates with faster Li^+ diffusion, which can lead to improved rate capability, higher power density, and better performance under high current conditions. Therefore, the substitution strategy used in $LiSr_{0.8}Ni_{0.1}Fe_{0.1}PO_4$ not only improves the structural tunability of the olivine framework but also offers promising characteristics for next-generation high-rate lithium-ion battery applications.

First-principles calculations have been extensively employed to predict the average voltage of Li deintercalation and intercalation in various compounds. The following equation is used to calculate the energy change of the individual Li amount at each deintercalation step in the $LiSr_{0.8}Fe_{0.1}Ni_{0.1}PO_4$ structure:[24]

$$\Delta E = E(Li_{x-y}Sr_{0.8}Fe_{0.1}Ni_{0.1}PO_4) + yE(Li) - E(Li_xSr_{0.8}Fe_{0.1}Ni_{0.1}PO_4) \quad (6)$$

where ΔE is the change in energy of the process where y(Li) atoms are extracted between the $LiSr_{0.8}Fe_{0.1}Ni_{0.1}PO_4$ layers,

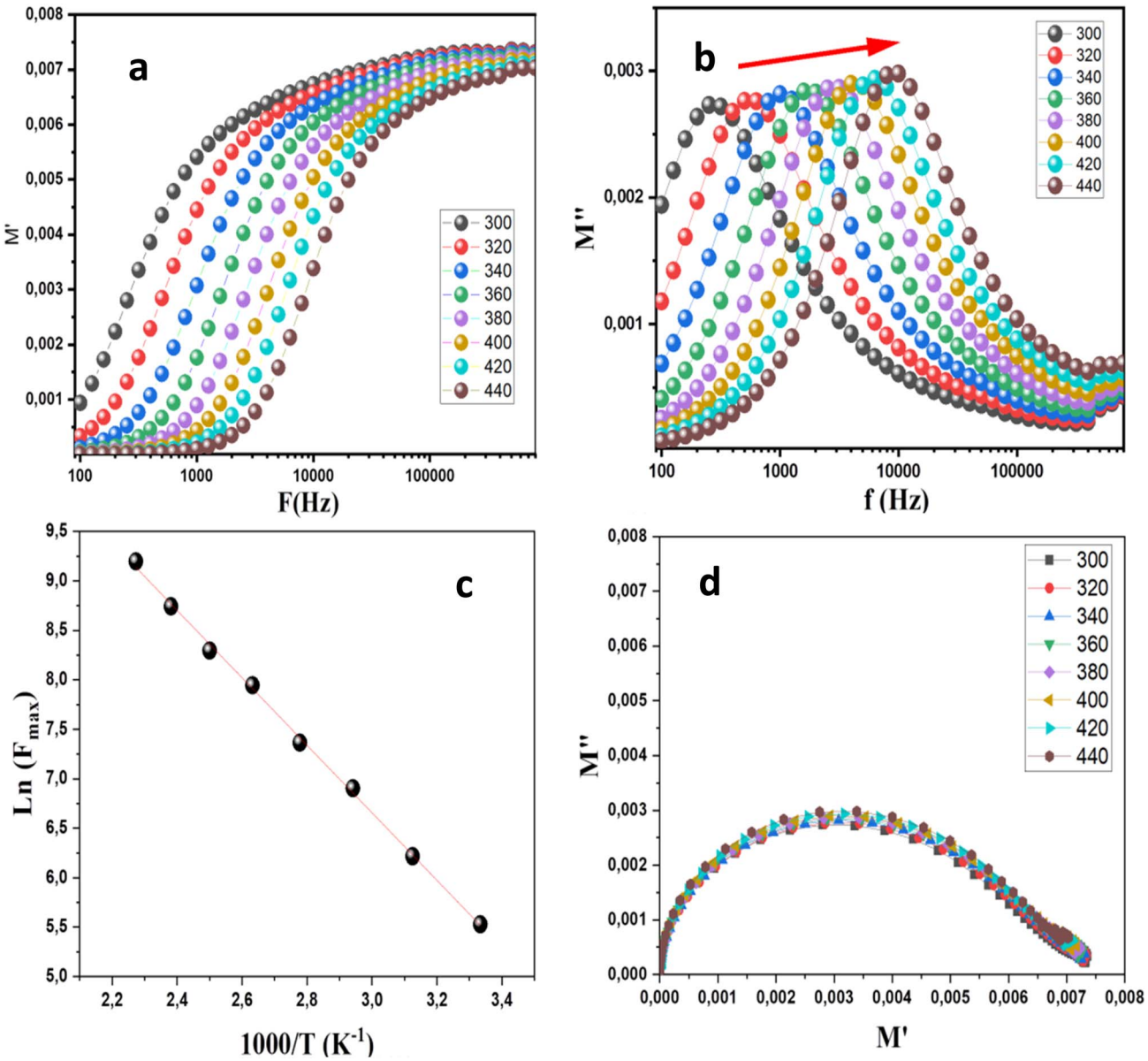

Fig. 8 Variation of the real (a) and imaginary (b) parts of the modulus, (c) the variation of ln(f_{max}) as a function of 1000/T, and (d) the scaling behavior of M''/M'.

$E(Li_{x-y}Fe_{0.1}Ni_{0.1}Sr_{0.8}PO_4)$ and $E(Li)$ and $E(Li_xFe_{0.1}Ni_{0.1}Sr_{0.8}PO_4)$ are the total energy of the $Li_{x-y}Fe_{0.1}Ni_{0.1}Sr_{0.8}PO_4$ and $Li_xFe_{0.1}Ni_{0.1}Sr_{0.8}PO_4$ samples respectively.

Accordingly, the cathode voltage/redox potential is calculated as follows:[37]

$$V = \frac{\Delta E}{ye} \quad (7)$$

V represents the cathode voltage/redox potential, e is the absolute value of the electron charge, and y is the amount of Li atoms extracted. At each deintercalation stage, Fig. 9b displays the average voltage/average potential determined using eqn (2). The voltage or potential required to extract the Li ions from $Li_{1-x}Fe_{0.1}Ni_{0.1}Sr_{0.8}PO_4$ ranged between 3.4 and 3.24 V.

In order to further assess the stabilities of the materials and understand the removal of Li in $Li_{1-x}Sr_{0.8}Fe_{0.1}Ni_{0.1}PO_4$ solid solutions, the formation energy per unit of formula was determined using the following equation:

$$Ef = E(Li_xFe_{0.1}Ni_{0.1}Sr_{0.8}PO_4) - xE(LiFe_{0.1}Ni_{0.1}Sr_{0.8}PO_4) - (1-x)E(Fe_{0.1}Ni_{0.1}Sr_{0.8}PO_4) \quad (8)$$

where $E(Li_xFe_{0.1}Ni_{0.1}Sr_{0.8}PO_4)$ is the partially deintercalated materials energy, $E(LiFe_{0.1}Ni_{0.1}Sr_{0.8}PO_4)$, and $E(Fe_{0.1}Ni_{0.1}Sr_{0.8}PO_4)$ are the pristine and entirely deintercalated structures energies, respectively. Except for $x = 1$, all the intercalation phase formation energy is negative in all the cases (Fig. 10).

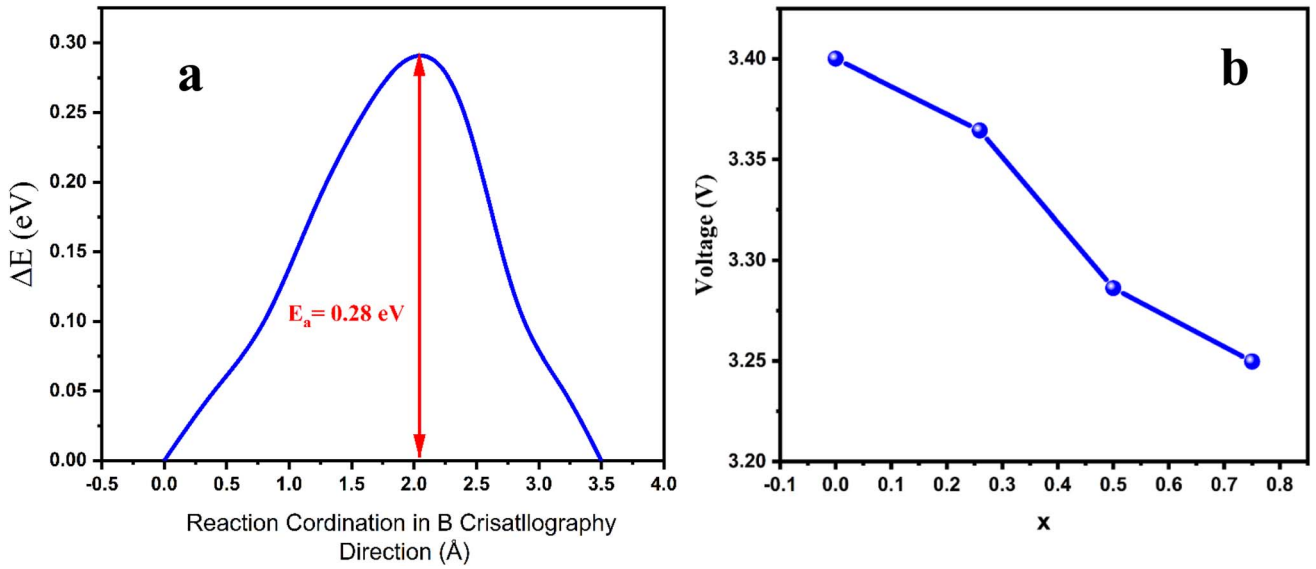

Fig. 9 (a) Plots of Li diffusion activation barrier along B-crystallographic axis for ($LiSr_{0.8}Fe_{0.1}Ni_{0.1}PO_4$), (b) deintercalation potentials (V) for $Li_{1-x}Fe_{0.1}Ni_{0.1}Sr_{0.8}PO_4$ (x = 0, 0.25, 0.5, 0.75).

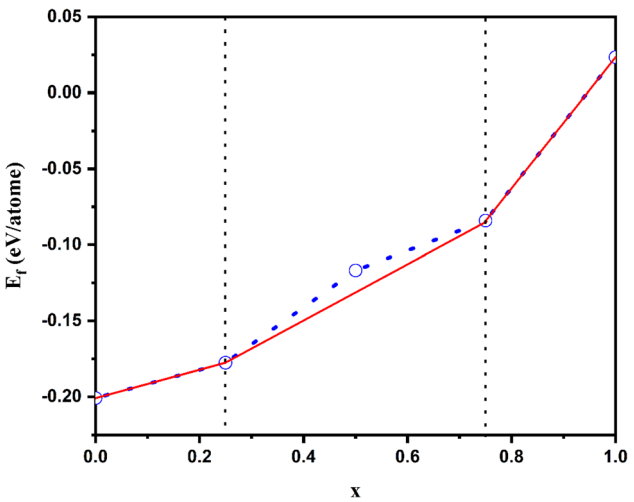

Fig. 10 The estimated *Ef* values for $Li_{(1-x)}Fe_{0.1}Ni_{0.1}Sr_{0.8}PO_4$ system as a function of concentration *x*. Data points located on the convex hull (solid red line) denotes stability against any type of decomposition. Metastable phases are represented by open circles on the blue dotted line. The concentration x is expressed in formula units (fu). $x = 1$ implies 32 Li atoms removed, respectively.

The stability criteria require that if $\Delta E > 0$, the material is considered metastable and can easily decompose into other compounds. However, if $\Delta E \leq 0$ the material is energetically stable.

The convex hull of these Ef values was obtained to identify which are the most energetically stable.[65] As depicted in Fig. 10, the solid red lines in the convex hull plots indicate the location of stable phases. The dashed blue lines indicate the meta-stable phases of the $Li_{1-x}Fe_{0.1}Ni_{0.1}Sr_{0.8}PO_4$ system. It is clear that three stable intermediate phases were obtained for all systems.

7. Conclusions

The $LiSr_{0.8}Fe_{0.1}Ni_{0.1}PO_4$ compound was synthesized *via* a sol–gel process. The X-ray diffraction pattern confirms a monoclinic structure with the $P2_1/m$ space group. To model the discharge process, Li extraction from the $LiSr_{0.8}Fe_{0.1}Ni_{0.1}PO_4$ lattice was examined using DFT calculations. Structural stability was maintained throughout deintercalation, with a semiconductor-to-semi-metallic transition observed during delithiation that enhances conductivity. Analysis of electrical properties revealed that the conduction mechanism follows the correlated barrier hopping (CBH) model at low temperatures and non-overlapping small polaron tunneling (NSPT) at high temperatures. The activation energy (E_a = 0.33 eV) calculated from conductivity data matches that derived from impedance measurements, confirming that both relaxation and conduction processes are governed by the same mechanism.

Conflicts of interest

The authors declare that they have no conflict interests.

Data availability

No primary research results, software or code have been included and no new data were generated or analysed as part of this review.

Acknowledgements

This research has been funded by Deputy for Research & Innovation, Ministry of Education through the Institutional Funding at University of Ha'il – Saudi Arabia through project number RG-23 118.

References

1 T. M. Gür, *Energy Environ. Sci.*, 2018, **11**, 2696–2767.
2 C.-X. Bi, L.-P. Hou, Z. Li, M. Zhao, X.-Q. Zhang, B.-Q. Li, Q. Zhang and J.-Q. Huang, *Adv. Energy Mater.*, 2023, **4**, 0010.
3 P. G. Bruce, S. A. Freunberger, L. J. Hardwick and J.-M. Tarascon, *Nat. Mater.*, 2012, **11**, 19–29.
4 A. A. İnada, S. Arman and B. Safaei, *J. Energy Storage*, 2022, **55**, 105661.
5 N. Nitta, F. Wu, J. T. Lee and G. Yushin, *Mater. Today*, 2015, **18**, 252–264.
6 M. Chen, P. Chen, F. Yang, H. Song and S. Liao, *Electrochim. Acta*, 2016, **206**, 356–365.
7 A. Bhatnagar, S. K. Pandey, V. Dixit, V. Shukla, R. R. Shahi, M. A. Shaz and O. N. Srivastava, *Int. J. Hydrogen Energy*, 2014, **39**, 14240–14246.
8 R. R. Shahi, R. K. Mishra, V. Shukla, A. Bhatnagar and O. N. Srivastava, *Int. J. Hydrogen Energy*, 2017, **42**, 29350–29359.
9 Y. F. Ye, Q. Wang, J. Lu, C. T. Liu and Y. Yang, *Mater. Today*, 2016, **19**, 349–362.
10 R. K. Mishra and R. R. Shahi, *J. Magn. Magn. Mater.*, 2020, **516**, 167342.
11 J. Kumar, R. R. Neiber, J. Park, R. Ali Soomro, G. W. Greene, S. Ali Mazari, H. Young Seo, J. Hong Lee, M. Shon, D. Wook Chang and K. Yong Cho, *Chem. Eng. J.*, 2022, **431**, 133993.
12 A. K. Padhi, K. S. Nanjundaswamy and J. B. Goodenough, *J. Electrochem. Soc.*, 1997, **144**, 1188.
13 Y. Ding, J. Fu, S. Zhang, X. He, B. Zhao, J. Ren, J. Zhong and Z. Liu, *Sep. Purif. Technol.*, 2024, **338**, 126551.
14 H. Wang, E. Lara-Curzio, E. T. Rule and C. S. Winchester, *J. Power Sources*, 2017, **342**, 913–920.
15 P. Koželj, S. Vrtnik, J. Boutbien, J. Luzar, A. Jelen, S. S. Parapari, P. Boulet, M.-C. de Weerd, G. Lengaigne, M. Wencka, V. Fournée, J. Ledieu, S. Šturm and J. Dolinšek, *Inorg. Chem.*, 2023, **62**, 6169–6180.
16 D. V. Trinh, M. T. T. Nguyen, H. T. M. Dang, D. T. Dang, H. T. T. Le, H. T. N. Le, H. V. Tran and C. D. Huynh, *Sci. Rep.*, 2021, **11**, 12280.
17 C.-C. Yang, Y.-T. Hsu, C. Karuppiah, J.-Y. Shih, Y.-S. Wu, Z.-H. Wu and S. J. Lue, *J. Alloys Compd.*, 2018, **750**, 945–958.
18 L. Liang, J. Jiang, F. Jiang, G. Hu, Y. Cao, Z. Peng and K. Du, *J. Alloys Compd.*, 2017, **695**, 1993–1997.
19 X. Li, L. Yu, Y. Cui, A. Li, H. Shao, Z. Shao, W. Zhang and Z. Shao, *Int. J. Hydrogen Energy*, 2019, **44**, 27204–27213.
20 N. Hua, C. Wang, X. Kang, T. Wumair and Y. Han, *J. Alloys Compd.*, 2010, **503**, 204–208.
21 H. Shu, X. Wang, W. Wen, Q. Liang, X. Yang, Q. Wei, B. Hu, L. Liu, X. Liu, Y. Song, M. Zho, Y. Bai, L. Jiang, M. Chen, S. Yang, J. Tan, Y. Liao and H. Jiang, *Electrochim. Acta*, 2013, **89**, 479–487.
22 P. Blaha, K. Schwarz, F. Tran, R. Laskowski, G. K. H. Madsen and L. D. Marks, *J. Chem. Phys.*, 2020, **152**, 074101.
23 A. Mabrouki, O. Messaoudi, M. Mansouri, S. Elgharbi and A. Bardaoui, *RSC Adv.*, 2021, **11**, 37896–37903.
24 A. E. Mabrouki, O. Messaoudi and L. H. Alfhaid, *Cryst. Growth Des.*, 2023, **23**, 6526–6534.
25 F. Zhou, M. Cococcioni, C. A. Marianetti, D. Morgan and G. Ceder, *Phys. Rev. B: Condens. Matter Mater. Phys.*, 2004, **70**, 235121.
26 A. Akyildiz, I. I. Aysan, Y. Z. Abdullahi, B. A. Hanedar, Z. D. Vatansever and F. Ersan, *Phys. Chem. Chem. Phys.*, 2024, **26**, 26566–26575.
27 M. F. Sgroi, R. Lazzaroni, D. Beljonne and D. Pullini, *Batteries*, 2017, **3**, 11.
28 G. K. P. Dathar, D. Sheppard, K. J. Stevenson and G. Henkelman, *Chem. Mater.*, 2011, **23**, 4032–4037.
29 M. F. Sgroi, R. Lazzaroni, D. Beljonne and D. Pullini, *Batteries*, 2017, **3**, 11.
30 K. Hoang and M. Johannes, *Chem. Mater.*, 2011, **23**, 3003–3013.
31 Q. Zhao, S. Zhang, M. Hu, C. Wang and G. Jiang, *Int. J. Electrochem. Sci.*, 2021, **16**, 211226.
32 A. Jain, G. Hautier, S. Ong, C. Moore, C. Fischer, K. Persson and G. Ceder, *Phys. Rev. B: Condens. Matter Mater. Phys.*, 2011, **84**, 045115.
33 S. Alshomar, M. Mansouri and A. Azhary, *Ceram. Int.*, 2024, **50**, 26402–26409.
34 Z. Liu and X. Huang, *Solid State Ionics*, 2010, **181**, 907–913.
35 S. Kanungo, A. Bhattacharjee, N. Bahadursha and A. Ghosh, *Nanomaterials*, 2022, **12**, 3266.
36 Y. Fang, Q. Liu, L. Xiao, X. Ai, H. Yang and Y. Cao, *ACS Appl. Mater. Interfaces*, 2015, **7**, 17977–17984.
37 R. S. Dima, P. M. Maleka, N. E. Maluta and R. R. Maphanga, *Materials*, 2022, **15**, 5280.
38 T. Tatarchuk, M. Bououdina, W. Macyk, O. Shyichuk, N. Paliychuk, I. Yaremiy, B. Al-Najar and M. Pacia, *Nanoscale Res. Lett.*, 2017, **12**, 1–11.
39 J. Massoudi, M. Smari, K. Nouri, E. Dhahri, K. Khirouni, S. Bertaina and L. Bessais, *RSC Adv.*, 2020, **10**, 34556–34580.
40 J. G. Lapping, S. A. Delp, J. L. Allen, J. L. Allen, J. W. Freeland, M. D. Johannes, L. Hu, D. T. Tran, T. R. Jow and J. Cabana, *Chem. Mater.*, 2018, **30**, 1898–1906.
41 M. S. Whittingham, *Chem. Rev.*, 2004, **104**, 4271–4302.
42 A. K. Padhi, K. S. Nanjundaswamy and J. B. Goodenough, *J. Electrochem. Soc.*, 1997, **144**, 1188.
43 J. B. Goodenough and Y. Kim, *Chem. Mater.*, 2010, **22**, 587–603.
44 C. Delacourt, P. Poizot, J.-M. Tarascon and C. Masquelier, *Nat. Mater.*, 2005, **4**, 254–260.
45 Y. Z. Abdullahi and F. Ersan, *RSC Adv.*, 2023, **13**, 3290–3294.
46 Y. Bakış, I. A. Auwal, B. Ünal and A. Baykal, *Ceram. Int.*, 2016, **42**, 11780–11795.
47 M. Beyranvand and A. Gholizadeh, *J. Mater. Sci.: Mater. Electron.*, 2020, **31**, 5124–5140.
48 S. M. El-Sayed, T. M. Meaz, M. A. Amer, H. A. E. Shersaby, S. M. El-Sayed, T. M. Meaz, M. A. Amer and H. A. E. Shersaby, *Phys. B: Condens. Matter.*, 2013, 137–143.
49 A. K. Jonscher, *Nature*, 1977, **267**, 673–679.
50 D. P. Almond, A. R. West and R. J. Grant, *Solid State Commun.*, 1982, **44**, 1277–1280.

51 N. F. Mott and E. A. Davis, *Electronic Processes in Non-crystalline Materials*, Clarendon Press ; Oxford University Press, Oxford; New York, 1979.
52 M. Pollak,Philos. Mag.-J. Theor. Exp. Appl. Phys., 1971, **23**, 519–542.
53 A. Ghosh, *Phys. Rev. B: Condens. Matter Mater. Phys.*, 1990, **41**, 1479–1488.
54 K. Funke, *Prog. Solid State Chem.*, 1993, **22**, 111–195.
55 A. Zaafouri, M. Megdiche, S. M. Borchani, O. Messaoudi, A. Mabrouki, L. Alfhaid, K. Dhahri and A. Dhahri, *J. Low Temp. Phys.*, 2023, **210**, 464–483.
56 K. K. Lily, K. Prasad and R. N. P. Choudhary, *J. Alloys Compd.*, 2008, **453**, 325–331.
57 R. Kumari, N. Ahlawat, A. Agarwal, S. Sanghi, M. Sindhu and N. Ahlawat, *J. Alloys Compd.*, 2016, **676**, 452–460.
58 H. S. Mohanty, T. Dam, H. Borkar, A. Kumar, K. K. Mishra, S. Sen, B. Behera, B. Sahoo and D. K. Pradhan, *Ferroelectrics*, 2017, **517**, 25–33.
59 S. R. Mohapatra, B. Sahu, M. Chandrasekhar, P. Kumar, S. D. Kaushik, S. Rath and A. K. Singh, *Ceram. Int.*, 2016, **42**, 12352–12360.
60 K. P. Padmasree, D. K. Kanchan and A. R. Kulkarni, *Solid State Ionics*, 2006, **177**, 475–482.
61 S. B. Yahya and B. Louati, *J. Alloys Compd.*, 2021, **876**, 159972.
62 F. S. Howell, R. A. Bose, P. B. Macedo and C. T. Moynihan, *J. Phys. Chem.*, 1974, **78**, 639–648.
63 I. Coondoo, N. Panwar, M. A. Rafiq, V. S. Puli, M. N. Rafiq and R. S. Katiyar, *Ceram. Int.*, 2014, **40**, 9895–9902.
64 T. V. S. L. Satyavani, B. Ramya Kiran, V. Rajesh Kumar, A. Srinivas Kumar and S. V. Naidu, *Eng. Sci. Technol. Int. J.*, 2016, **19**, 40–44.
65 *Boron phosphide (BP) biphenylene and graphenylene networks as anode and anchoring materials for Li/Na-ion and Li/Na–S batteries – ScienceDirect*, **https://www.sciencedirect.com/science/article/abs/pii/S0169433224008092?via%3Dihub**, (accessed July 26, 2025).